AGU PUBLICATIONS

JGR

Journal of Geophysical Research: Space Physics

RESEARCH ARTICLE

10.1002/2014JA020522

Key Points:

- Azimuthal SCW dynamics nicely order various substorm signatures in the tail
- AMPERE confirms quadrupolar FAC source of SCW supporting two-loop model
- SCW2L model outperforms other models in describing dipolarized configuration

Supporting Information:

- Readme
- Animation S1
- Animation S2
- Figure S1
- Figure S2
- Figure S3

Correspondence to:
V. A. Sergeev,
victor@geo.phys.spbu.ru

Citation:
Sergeev, V. A., et al. (2014), Event study combining magnetospheric and ionospheric perspectives of the substorm current wedge modeling, *J. Geophys. Res. Space Physics*, *119*, 9714–9728, doi:10.1002/2014JA020522.

Received 19 AUG 2014
Accepted 8 NOV 2014
Accepted article online 13 NOV 2014
Published online 9 DEC 2014

Event study combining magnetospheric and ionospheric perspectives of the substorm current wedge modeling

V. A. Sergeev[1], A. V. Nikolaev[1], M. V. Kubyshkina[1], N. A. Tsyganenko[1], H. J. Singer[2], J. V. Rodriguez[2,3], V. Angelopoulos[4], R. Nakamura[5], S. E. Milan[6], J. C. Coxon[6], B. J. Anderson[7], and H. Korth[7]

[1]Earth's Physics Department, St. Petersburg State University, St. Petersburg, Russia, [2]NOAA Space Weather Prediction Center, Boulder, Colorado, USA, [3]NOAA National Geophysical Data Center, Boulder, Colorado, USA, [4]Department of Earth, Planetary, and Space Sciences, University of California, Los Angeles, California, USA, [5]Space Research Institute, Austrian Academy of Sciences, Graz, Austria, [6]Department of Physics and Astronomy, University of Leicester, Leicester, UK, [7]Johns Hopkins University Applied Physics Laboratory, Laurel, Maryland, USA

Abstract Unprecedented spacecraft and instrumental coverage and the isolated nature and distinct step-like development of a substorm on 17 March 2010 has allowed validation of the two-loop substorm current wedge model (SCW2L). We find a close spatiotemporal relationship of the SCW with many other essential signatures of substorm activity in the magnetotail and demonstrate its azimuthally localized structure and stepwise expansion in the magnetotail. We confirm that ground SCW diagnostics makes it possible to reconstruct and organize the azimuthal spatiotemporal substorm development pattern with accuracy better than 1 h magnetic local time (MLT) in the case of medium-scale substorm. The Active Magnetosphere and Planetary Electrodynamics Response Experiment (AMPERE)-based study of global field-aligned current distribution indicates that (a) the SCW-related field-aligned current system consists of simultaneously activated R1- and R2-type currents, (b) their net currents have a R1-sense, and (c) locations of net current peaks are consistent with the SCW edge locations inferred from midlatitude variations. Thanks to good azimuthal coverage of four GOES and three Time History of Events and Macroscale Interactions during Substorms spacecraft, we evaluated the intensities of the SCW R1- and R2-like current loops (using the SCW2L model) obtained from combined magnetospheric and ground midlatitude magnetic observations and found the net currents consistent (within a factor of 2) with the AMPERE-based estimate. We also ran an adaptive magnetospheric model and show that SCW2L model outperforms it in predicting the magnetic configuration changes during substorm dipolarizations.

1. Introduction

As a part of magnetotail reconfiguration during substorms, the near-Earth magnetosphere is altered by the magnetic field dipolarization and associated particle acceleration and injection processes that operate in azimuthally localized sectors of near-Earth space. These processes may repeat several times in the course of a moderate-to-strong substorm. More than 40 years ago, *McPherron et al.* [1973] suggested the substorm current wedge (SCW) as a simple 3-D current system, consistent with observed magnetic signatures in the near tail and on the ground. The system was originally visualized as a region 1-type azimuthal current loop with upward/downward field-aligned currents on duskward/dawnward edges of the auroral bulge, completed by a westward current in the ionosphere and an equal eastward current in the equatorial magnetosphere (the R1-type loop). Such a single-loop SCW model nicely explains the observed magnitude and polarity of the bay-like midlatitude magnetic variations and was therefore suggested as a tool to monitor the intensity and location of substorm currents [*Horning et al.*, 1974; *Sergeev et al.*, 1996a; *Chu et al.*, 2014]. Concurrent perturbations in the auroral zone and in the magnetosphere are more structured and complex, so more research is needed to fully understand the configuration and dynamics of the associated current system.

While our understanding of the SCW has greatly improved owing to MHD simulations of tail reconnection [e.g., *Birn and Hesse* [2014]; L. Kepko et al., Substorm current wedge revisited, submitted to *Space Science Review*, 2014], observational studies of the large-scale substorm effects in the magnetotail have been less productive for two reasons. The first reason is the sporadic, dynamic, and three-dimensional nature of magnetotail activity during substorms can easily be missed because of the sparsity of the existing

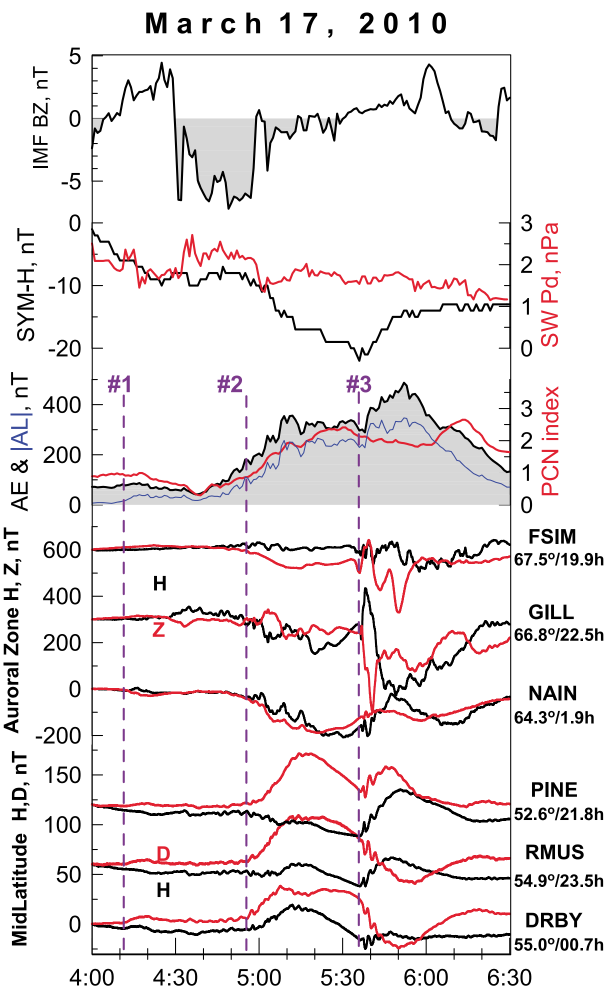

Figure 1. Summary of activity on 17 March 2010. From top to bottom: IMF B_z variations (OMNI data), solar wind flow pressure, and ground *SYM-H* index; *AE* index and northern *PC* index; nightside auroral zone magnetograms; nightside midlatitude magnetograms. Station geomagnetic latitude and MLT at 05 h UT are also shown.

spacecraft fleet. The second reason is that simple and flexible SCW models for interpreting sparse spacecraft observations have appeared only recently [*Sergeev et al.*, 2011].

Two recent developments provide new opportunities for studying the substorm current wedge. First, an updated computational SCW model was suggested and tested with the purpose to describe the distribution of dipolarization magnitudes in the near-Earth space and at midlatitudes [*Sergeev et al.*, 2014]. This model can be used to obtain information on the intensity and location of the SCW currents using combined magnetospheric and ground-based observations. In addition to the standard R1-type loop, it includes a loop of opposite polarity (i.e., of R2 type), located at the inner edge of the dipolarization region in the magnetosphere. Such an additional loop has been recently inferred in the Rice Convection Model-Equilibrium self-consistent simulations of flow burst injections [*Yang et al.*, 2012] (Figure 2), and it is also consistent with 3-D MHD simulation analyses by *Birn and Hesse* [2014, Figure 14]. Validation of the two-loop substorm current wedge model (SCW2L) model is still a challenging task that is needed before introducing in practice. The other new tool, the Iridium satellite constellation-based “Active Magnetosphere and Planetary Electrodynamics Response Experiment” (AMPERE) [*Anderson et al.*, 2014] makes it possible to derive 2-D pattern of field-aligned substorm currents in the ionosphere and, hence, offers an effective method to validate the SCW2L model [e.g., *Clausen et al.*, 2013; *Murphy et al.*, 2013].

To further study the SCW configuration and details of its relationship to magnetospheric and ionospheric processes, as well as to validate the SCW2L model, in this paper we analyze magnetospheric and ionospheric observations made during a sequence of three consecutive substorm activations, all observed with unprecedented coverage and completeness on 17 March 2010 with four GOES and four Time History of Events and Macroscale Interactions during Substorms (THEMIS) spacecraft. A key component of our study is the reconstruction of the SCW azimuthal location and dynamics obtained from the interpretation of midlatitude bay-like magnetic variations, which usually provide the clearest and most complete view of the SCW dynamics. Among the questions to be explored are the following: (1) What is the spatiotemporal relationship of the derived SCW to different features of substorm activity in the magnetotail, and how accurately can the model predict the azimuthal location of dipolarization/injection activity at geosynchronous orbit and its evolution? (2) How consistent are the ionospheric and magnetospheric manifestations of the double-loop (R1 and R2) pattern and the estimates of the net current inferred from AMPERE field-aligned current (FAC) observation and obtained from the SCW2L model? (3) How does the SCW2L model compare with other

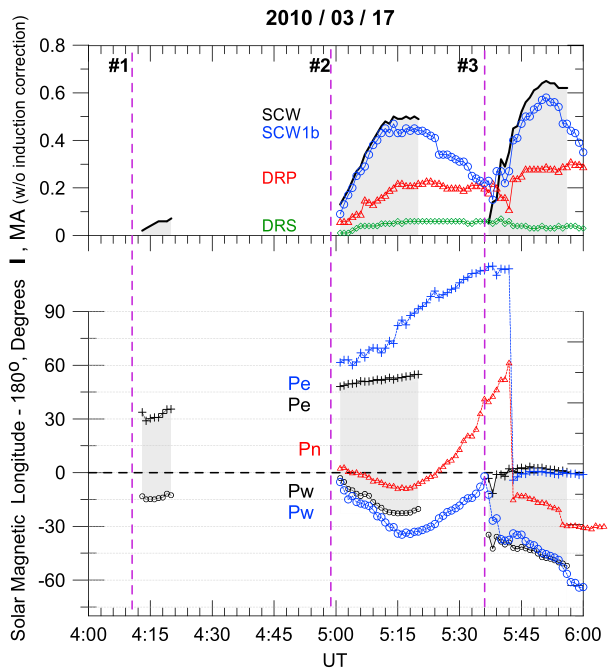

Figure 2. Results of the midlatitude magnetogram inversion for the 17 March 2010 event. (top) Time variations of total SCW and DRP currents (with no correction for the induction effects); (bottom) azimuthal dynamics of SCW and DRP field-aligned currents. Inferred longitudes of east (Pe) and west (Pw) SCW edges are shown together with the longitude of nightside edge of the DRP system. Black lines show results after subtracting the reference level at the beginning of each activation #1, #2, and #3 separately. Results with a single reference level at #2 applied for both activations #2 and #3 are shown by blue (SCW) and red (DRP) color to illustrate sensitivity to the different choices of the reference level. See Animation S1 for comparison of observed and modeled magnetic perturbations.

existing models (e.g., the adaptive Tsyganenko-type models) in describing the spatial deformation of the near-Earth magnetic field?

2. Reconstruction of Substorm Dynamics in the Magnetosphere

2.1. Event Description: SCW Reconstruction From Midlatitude Ground Magnetic Observations

After a 5 h long geomagnetically quiet period under northward interplanetary magnetic field (IMF) conditions, magnetospheric activity was initiated by two 0.5 h long episodes of southward IMF (starting at 0330 UT (not shown) and 0430 UT), followed by ground magnetic activity as shown in Figure 1. Three activations were well pronounced in the ground-based and magnetospheric observations. The first activation (#1) showed a weak ground effect. Two other activations started after the end of a period with strong southward IMF and showed quite intense and distinct bay-like midlatitude perturbations, occupying different local time sectors. Namely, activation #2 developed mostly in the postmidnight sector (westward electrojet effects were seen at NAIN and a clear midlatitude bay at DRBY), whereas during activation #3 the activity was shifted to premidnight sector (and is now clearly seen at FSIM and PINE). Both activations were seen at the near-midnight stations (GILL and RMUS).

Quantitative reconstruction of spatial dynamics is possible, based on interpretation of the bay-like midlatitude magnetic variations. We use a version of the inversion technique described by *Sergeev et al.* [1996a], which is suitable for isolated and sharply defined substorm activations. A limitation of the method is that the reference level just before the start of the magnetic bay (which differs from one event to another) needs to be subtracted from the observed variations. The resulting horizontal perturbation vectors are fitted to those predicted by a three-component wire-type model that includes a substorm current wedge (SCW), a partial ring current (DRP), and a symmetric ring current. As the input, we use H and D component magnetograms from 19 midlatitude INTERMAGNET stations, distributed around the globe. The distribution of stations, the disturbance pattern, and the good agreement between the model and observations are illustrated in Animation S1 in the supporting information. The inferred parameters are displayed in Figure 2. For activation #3, one can compare the results with subtracting different reference levels (taken either at #2 or at #3 starting points). These results disagree at the start of activation #3, when remnants of the preexisting wedge are observed together with the quickly growing new wedge in the premidnight sector (see Animation S1), but soon the new wedge prevails over the previous one, and both results closely agree with each other near the peak of the activation and thereafter.

Figure 2 confirms that the first event (#1) was of low intensity ($<$ 0.1 MA) and that strong activations #2 and #3 occupied different azimuthal sectors, with only a small overlap between them near the midnight. In agreement with Figure 1, the wedge was mostly developing in the postmidnight sector for #2, and in the premidnight sector for #3. Such large step-like displacements of the substorm active region are not

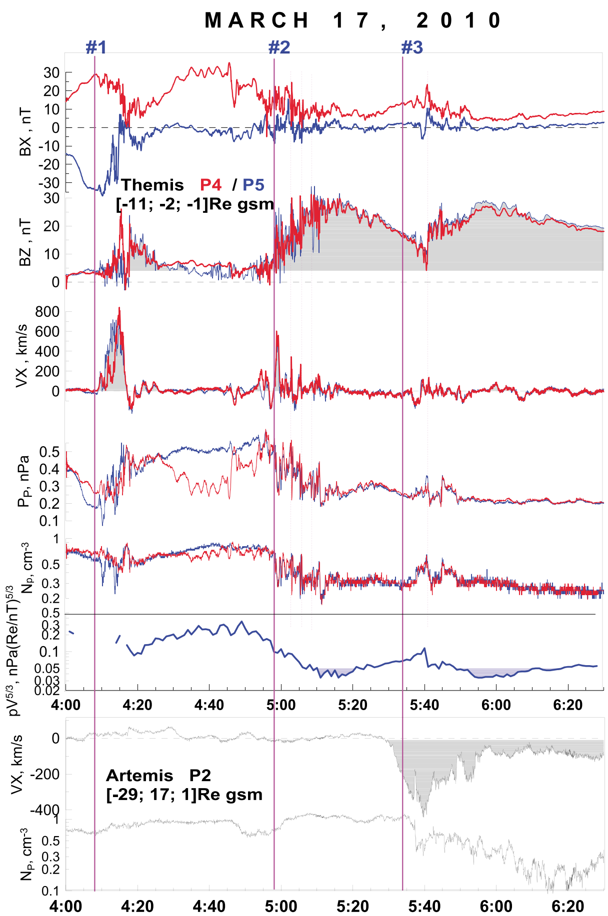

Figure 3. Plasma sheet observations from THEMIS P4, P5, and Artemis P2 spacecraft. Onsets of ground SCW activations are marked by the vertical lines.

uncommon in substorms, and they are helpful for our goal to test how well the SCW dynamics represents the azimuthal dynamics of various magnetospheric manifestations, that is, to show their connection with the substorm current wedge. Azimuthal coverage of magnetospheric spacecraft is excellent for such a task in this event.

2.2. Observations in the Plasma Sheet

THEMIS observations in the magnetotail are presented in Figure 3. Current understanding of substorm dipolarizations relates them to magnetic reconnection, in which magnetic field energy stored in the tail is converted to the plasma flow and thermal energy [*Birn and Hesse*, 2014; *Angelopoulos et al.*, 2013; L. Kepko et al., submitted manuscript, 2014]. The magnetic reconnection is known to proceed in azimuthally narrow regions across the tail [*Ieda et al.*, 2008], sending fast Earthward and tailward outflows, confined to the corresponding "magnetic field line planes" [*Angelopoulos et al.*, 2013]. Such azimuthally confined (or, sectorial) organization of the reconnection activity is usually difficult to monitor, and our study provides nice material to demonstrate this feature.

The midtail observations in the duskside plasma sheet at [−29; 17; 1] R_E came from the Artemis AP2 probe (Figure 3, bottom). According to Figure 4, during the first two events the spacecraft was outside the active SCW sector. Consistent with that, fast flows or reconnection signatures were absent at Artemis, indicating that the tail plasma sheet was undisturbed at that time. During that time period the probe did not exit from the plasma sheet, as confirmed by the large plasma density. In sharp contrast, during activation #3 the AP2 probe showed fast tailward flow and turbulent magnetic field (not shown) inside the flow burst, being now in radial conjunction with the premidnight SCW location at that time. This flow burst started about 6 min before the SCW sharp onset, which is also consistent with the reconnection outflow being the ultimate source of the dipolarizations [*Angelopoulos et al.*, 2013].

In the upper panels, two closely spaced THEMIS probes, P4 and P5 (separated in the Z coordinate by 0.6 R_E), provide an illustration of magnetotail activity at $r \sim 11$ R_E, i.e., at the interface of the dipole-like and tail current sheet domains. The B_x component difference at the two vertically separated P4 and P5 probes (d$Z \sim 0.6$ R_E) allows one to evaluate the current density in the plasma sheet. Unlike the AP2 probe, these spacecraft stayed inside the active SCW sector during the events #1 and #2 (see Figure 4). In both cases the measurements show the preconditioning of the magnetotail, namely, thin current sheet features before the dipolarization onset. In particular, the electric current density was especially large (proportional to $(B_{x4} - B_{x5})/\mathrm{d}Z$, up to 15 nA/m^2) prior to the first event, indicating the formation of a thin current sheet. The difference $(B_{x4} - B_{x5})$ droped down during the following dipolarizations, illustrating that current disruption and plasma sheet expansion were closely related to the dipolarization signatures in the near-tail region [*McPherron et al.*, 1973; L. Kepko et al., submitted manuscript, 2014]. Another basic dipolarization-associated phenomenon, the earthward plasma flow and flux transport [*McPherron et al.*, 2011], is also seen. V_x was generally smaller in event #2 compared to #1, but B_z was larger, such that the $V_x \times B_z$ component of the flux

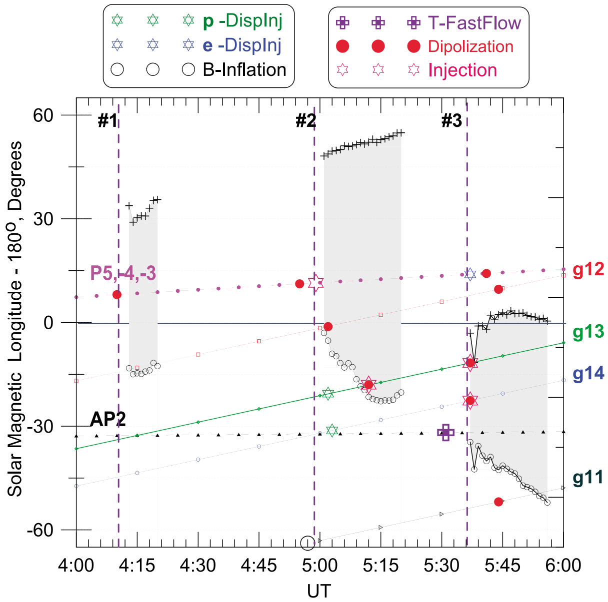

Figure 4. Spatial development of substorm current wedge (from midlatitude magnetogram inversion shown in Figure 2) with overlapped spacecraft trajectories. Commencement of substorm activity signatures at different spacecraft is shown by different symbols (see legend at the top of the figure, DispInj indicates energy-dispersed injections, *p* and *e* correspond to protons and electrons) to illustrate their relationship to the SCW dynamics.

transport had comparable peak values, with E_y up to 10 mV/m, in both events. This event also provides an excellent illustration of another associated phenomenon, plasma depletion, which is a well-known property of the plasma sheet bursty bulk flows and reconnection outflow. Simultaneous drops in plasma density and pressure P_p at 11 R_E shows that plasma tubes transported into the dipolarized region are depleted compared to the ambient plasma (see also AP2 observations of the density drop in the high-speed tailward flow in Figure 3). This dipolarization-associated plasma and entropy ($pV^{5/3}$) depletion, while created within several minutes, may persist for a longer time after the dipolarization. In drastic contrast to first two events, there was no dipolarization, no fast flows, no large flux transport, and no progressing plasma depletion (the density stays elevated at the preonset level) during event #3, when THEMIS probes stayed just eastward of the activated premidnight portion of the SCW, according to Figure 4.

2.3. Geosynchronous Observations: Association of Injections, Dipolarizations, and the Midlatitude SCW

In this event, we had remarkable coverage at geosynchronous orbit with four NOAA Geostationary Operational Environmental Satellites (GOES) spacecraft, distributed near midnight over a 4.5 h magnetic local time (MLT) sector and providing magnetic field measurements of the azimuthally localized dipolarizations. Two of them (g13 and g14) also provided energetic particle observations allowing one to distinguish between dispersionless particle injections and drifting particle clouds (energy dispersed injections). Figures 3–5, taken together, provide an excellent textbook example that shows how different magnetospheric substorm signatures in the inner magnetosphere correspond to each other.

Considering activations #2 and #3, one sees that the dipolarizations occupied the same MLT sector as the SCW, obtained in the ground magnetogram inversion, and they showed similar dynamics (see *McPherron et al.* [1973], *Singer et al.* [1985], and *Nagai* [1982] for previous observations). Indeed, the large bay-like increases of H_p (or B_z), a basic signature of the dipolarization (red shading), were only observed when the spacecraft entered the wedge sector in Figure 4 (P5 and g12 in the event #2 and g13 and g14 in the event #3). Delayed dipolarizations were observed when the spacecraft crosses the edge of the westward expanding wedge (g13 in event #2 and g11 in event #3) or eastward expanding edge (like P5 and g12 in event #3). Near the expanding edges of the SCW, the bay-like dipolarizations were less intense than those observed in the SCW center and the association between the midlatitude SCW edge location and the spacecraft location during delayed dipolarization onset had a roughly 1 h MLT accuracy.

Energetic particle observations from 30 keV to hundreds keV were available at three longitudes thanks to THEMIS P5 and GOES 13 and GOES 14 observations (data from Magnetospheric Electron and Magnetospheric Proton Detectors above 80 keV for protons and above 30 keV for electrons [see, e.g., *Hanser*, 2011]). Figure 5 (and Figure S1) nicely demonstrates a known feature of how the ion/electron content of injections varies in longitude and how they correspond to the dipolarization region [see, e.g., *Birn et al.*, 1997]. However, in [*Birn et al.*, 1997], the relation to the dipolarization region was assumed rather than shown since the magnetic field was not directly measured at Los Alamos National Laboratory spacecraft. Inside the SCW/dipolarization region both protons and electrons showed simultaneous flux increases at

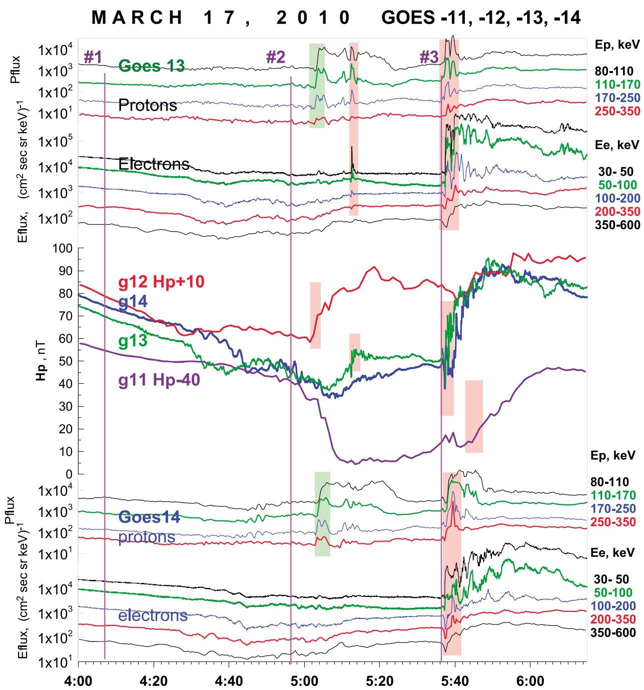

Figure 5. (middle) Geosynchronous observations of dipolarizations and energetic particle injections (at (top) GOES 13 and at (bottom) GOES 14). Vertical color strips indicate onsets of dipolarizations and dispersionless injections (red) and energy dispersed injections (green).

all energies (dispersionless injections), e.g., P5 in event #2 and g13 and g14 in event #3. Westward of the dipolarization region, only proton flux increases were observed with a time delay from high to low energy (energy-dispersed protons injection), with an additional delay at the more westward spacecraft, e.g., g13 and g14 in event #2 (see a high-resolution data in Figure S2). Eastward of the dipolarization region only energy-dispersed electron injection was observed (e.g., at P5 in event #3; Figure S1). One may also notice that during the sharp injection feature at the dipolarization front in activation #3, the flux droped out simultaneously in the highest energy (> 100 keV) electron channels, indicating the birth of the drifting electron hole phenomenon which will subsequently drift eastward in longitude [*Sergeev et al.*, 1992].

Radial dynamics adds some complexity to this simple picture, which should be mentioned for completeness. An apparent exception is that during weak event #1, no dipolarization signatures (at g12, which is inside the SCW) and no particle injection signatures were seen at geostationary orbit, while they were reliably registered at 10 R_E by the THEMIS probes. This is explained by the dependence of injection probability at the geosynchronous location on the magnetotail stretching, which is very low for B_z (or Hp) larger than ~ 70 nT at GEO (see Figure 12 in *Sergeev et al.* [2014]). At GOES 12 B_z was about 70 nT (close to the injection limit) before activation #1, whereas it was about 50 nT (much below this limit) for activation #2, which explains the difference. Another feature worth noting is the propagation time delay between the flow burst (dipolarization and injection features) registration at 10 R_E and its appearance at geosynchronous orbit. The delay was about 3–4 min for the most robustly tracked activation #2 (see Figure S2).

To conclude this section, we demonstrate that SCW detection based on midlatitude magnetogram inversion allows one to organize very well various substorm signatures in the midtail and near tail, indicating the azimuthal (sectorial) organization of the activity, with different sectors activated at different times. Also in this case, as a result of SCW expansion, the association between the midlatitude SCW edge location and the spacecraft location at the dipolarization onset had a roughly 1 h MLT accuracy.

3. AMPERE's View of the Substorm Current Wedge

A new opportunity to map the ionospheric portion of field-aligned currents is now available due to the success of the AMPERE project [*Anderson et al.*, 2014]. AMPERE utilizes about 70 satellites from the Iridium constellation to infer the global structure of FACs from vector measurements of the magnetic field in both the Southern and Northern Hemispheres. With the satellites distributed in six circular orbital planes at ~ 780 km altitude, AMPERE is able to determine the FAC spatial distribution in each hemisphere with a spatial resolution in geomagnetic coordinates of 3° in latitude and 2 h of magnetic local time (MLT). The quasi-stationary FAC maps are constructed in 10 min time windows, required for the constellation to sample the entire Northern or Southern Hemispheres.

Figure 6 shows the (Figures 6a and 6d) Iridium raw and (Figures 6b and 6e) fitted magnetic perturbations and the (Figures 6c and 6f) resulting field-aligned current distribution for the (Figures 6a–6c) Northern

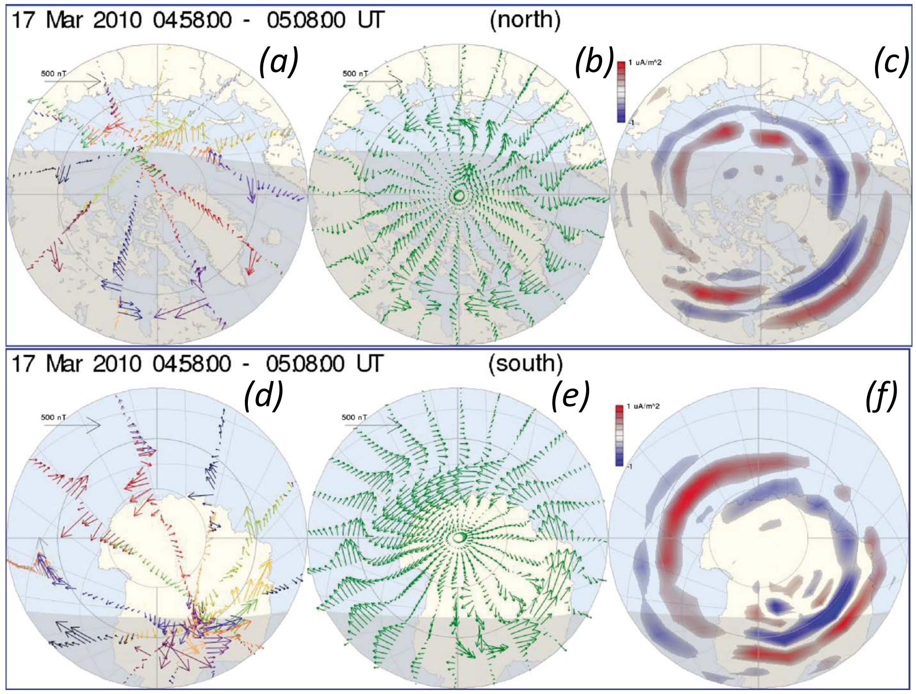

Figure 6. (a and d) AMPERE maps of *B* field perturbations measured along spacecraft trajectories; and fitted distributions of (b and e) magnetic perturbations and of (c and f) FAC densities (red: upward FAC; blue: downward FAC) for Northern (Figures 6a–6c) and Southern (Figures 6d–6f) Hemispheres; grey shadow shows the dark portions of the ionosphere.

and (Figures 6d–6f) Southern Hemispheres. It illustrates a few important differences concerning observations in the Northern and Southern Hemispheres. First, at the UT shown, the northern nightside auroral zone is crossed by spacecraft in a more regular way (with roughly equidistant nearly meridional crossings, Figure 6a), than the Southern Hemisphere premidnight and postmidnight sectors which are crossed in different directions and less homogeneously (Figure 6d). Second, there is a large contrast in solar illumination between the hemispheres. The southern auroral zone is almost fully illuminated, whereas the nightside (18:00:06 MLT) part of northern auroral zone is entirely in darkness and the ionospheric conductivity here is controlled by the particle precipitation during this substorm.

AMPERE data were further processed to calculate the total upward and total downward currents (I1 and I2), as well as their sum (I1 + I2), i.e., the net current in 1 h wide MLT meridional strips at GM latitudes between 55° and 80°. Figure 7a shows the variation of total currents in the Northern Hemisphere. Before 0430 UT the northern currents are at marginal level (whereas in the sunlit Southern Hemisphere they are already strong under the action of southward IMF). They start to grow after 0430 UT, most strongly during SCW activations #2 and #3. These currents mostly increase on the nightside, as seen by comparing the I1 total currents in 13–23 (or 01–11) MLT sectors with those in 18–23 (or 01–06) MLT sectors. At their peaks, the nightside I1 currents reach the 1 MA level. The net current increase is much smaller, indicating that the R1-type and R2-type currents grow together and are roughly balanced during the SCW growth, consistent with the pattern shown in Figure 6c. However, the value of Figure 7a is limited for SCW studies, as it ignores the asymmetric azimuthal distribution and dynamics of the SCW currents.

Figure 7b shows the azimuthal distribution of net currents obtained during the peak epochs of two SCW activations. Comparing the peak epochs with the distributions obtained just before the activation onset (grey lines) helps to identify changes in the azimuthal distribution of the net current. In both activations, the net current patterns (both total pattern and the color-coded differential pattern, i.e., the difference between black and grey lines) reveal the enhanced upward (positive) current to the west and the enhanced downward current to the east of the SCW center. Their peak locations are roughly consistent (with 2 h MLT resolution) with the SCW edge locations inferred from the magnetogram inversion results shown in Figure 2. Similar relative patterns of azimuthally displaced net upward current (on the west side) and net

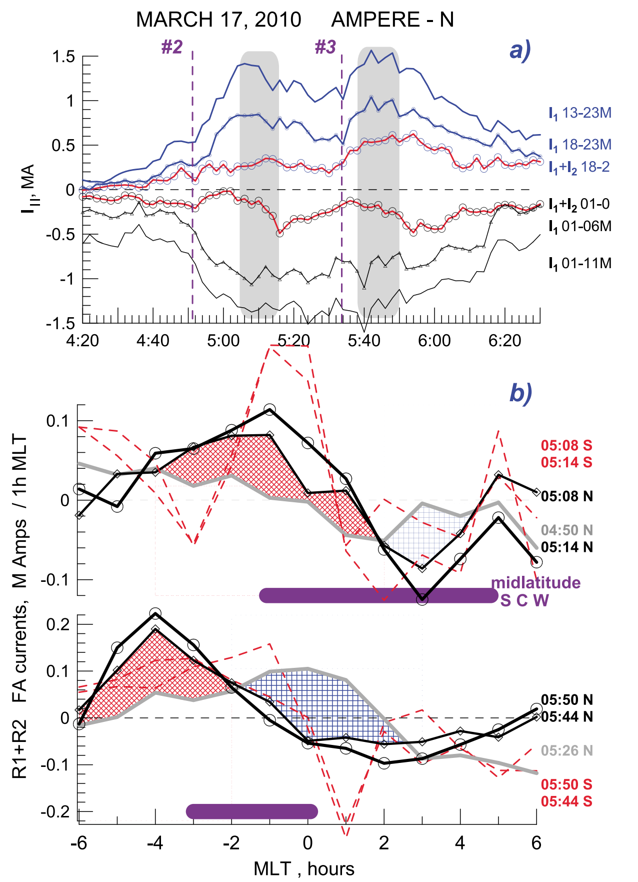

Figure 7. (a) Variations of the total region 1-type currents (I1) and the net current (I1+I2) on dawn and dusk sides of the auroral zone (55 to 80° GMLat) in the Northern Hemisphere. (b) Azimuthal distributions of net currents near the SCW peak epochs (black lines in the Northern Hemisphere and red lines in the Southern Hemisphere) together with their distribution before the SCW activation (grey line, shown only for Northern Hemisphere). Horizontal bars show the azimuthal extent of the SCW obtained from magnetogram inversion near the corresponding SCW peaks.

downward current (on the east side) have been recently obtained by *Murphy et al.* [2013], who showed in addition that the intensified westward auroral electrojet was mostly confined in longitude between the peaks of the net current. This gives us an opportunity to visualize and extract from the total FAC (evaluated from AMPERE's data) its part corresponding to the substorm current wedge. (The total pattern includes also the global Iijima-Potemra two-sheet FAC pattern, as well as partial ring current-related component and possible contributions from other sources.)

The total current data from the Southern Hemisphere (red lines) look qualitatively similar although more irregular, possibly reflecting the uneven coverage of the Southern Hemisphere crossings (Figure 6d). This underscores uncertainties in the AMPERE method, which is sensitive to the coverage details. Quantitative estimation of additional net current from AMPERE data (after subtracting the preceding values, that is, the red/blue areas shown in Figure 7b) gives for the Northern Hemisphere 0.25/−0.11 MA at 0508 UT and 0.37/−0.40 MA at 0544 UT (plus/minus correspond to the total net upward/downward currents). These values can be used as AMPERE-based proxies for the net SCW current intensity. In the Southern Hemisphere estimates have similar magnitudes with 0.32/−0.08 MA at 0508 UT and 0.29/−0.30 MA at 0544 UT. While the derived upward/downward net current values are nearly balanced for activation #3, in event #2 the net upward current is larger than the net downward current, and this is the case in both hemispheres. To understand this imbalance, one may remember that during activation #2 the partial ring current (DRP) displayed a significant growth according to magnetogram inversion results (Figure 2). According to Figure 2, the DRP-related upward FAC current is located near the midnight, inside of the SCW sector. The total DRP current inferred from midlatitude data was about 0.1 MA (after applying the induction correction), which roughly accounts for the observed unbalance. With this correction, the increase of net SCW current in one hemisphere is estimated from AMPERE method at about 0.2 MA during activation #2 and about 0.3-0.4 MA during activation #3.

To conclude this section, AMPERE data related to the large-scale FACs in the Northern Hemisphere show reasonable agreement with SCW parameters obtained from the magnetogram inversion method. The data show consistent temporal variations of total electric current as well as similar spatial locations and distributions of the net currents (Figures 2 and 7). In addition, AMPERE data assure us that in this case the SCW is a combination of rather strong R1-type and (more equatorward) R2-type FACs (Figure 6c) so the SCW has a quadrupolar FAC source, with the net current being of R1 type.

4. Magnetospheric View of the Substorm Current Wedge: Validation of the SCW2L Model

The unprecedented coverage of the inner magnetosphere by four geostationary spacecraft supported by THEMIS spacecraft at 11 Re allowed us to evaluate the SCW intensity from magnetic observations and to compare the result with ionospheric observations. Consistent with AMPERE results, we use the SCW2L interpretational model including two pairs of filamentary field-aligned currents (poleward R1 loop and more equatorward R2 loop), presented, tested, and extensively discussed recently by *Sergeev et al.* [2014]. Our main task in this section is to obtain the intensities of both R1 current (I1) and R2 current (I2), which are consistent with the measured magnetospheric dipolarization amplitude (dB_z) as well as with dX and dY midlatitude perturbations. As discussed in *Sergeev et al.* [2014], the dipolarization magnitude in the inner magnetosphere is mostly sensitive to (and allows to evaluate) the magnitude of I1 current, whereas the midlatitude variations are sensitive to the net current (I1 + I2), so their combination allows us to evaluate both I1 and I2 components.

Because of the scarcity of magnetospheric spacecraft observations, the model should be as simple as possible and additional (midlatitude) ground-based magnetic observations should be used. In particular, in the following computations the azimuthal locations of the SCW (and DRP) field-aligned currents are simply taken from the inversion of midlatitude magnetograms shown in Figure 2, and they are not modified afterward. In the SCW2L model, both SCW loops (R1 and R2) are assumed to occupy the same azimuthal sector (the sector between the Pw and Pe longitudes of the SCW edges obtained from midlatitude analyses, see Figure 2). Whereas in paper 1 we had a conjunction of five spacecraft spread radially between 6 and 12 R_E, and we were able to resolve the equatorial locations of R2 current and (to some extent) of the R1 current, in our case the spacecraft stay only at two distances (6.6 and 11 R_E). Therefore, we chose to fix these locations (RT2 and RT1) at distances 5.5 and 15 R_E, correspondingly. As demonstrated in paper 1, the variations of RT2 or RT1 have a minor influence on the dipolarization amplitude unless they are close to (less than roughly $\sim 1\ R_E$ from) the location of observing spacecraft. In our case we select the filament-type current model (with the filament size of $\sim 1\ R_E$ in the region of interest) with field-aligned currents flowing along realistic field lines (see paper 1 for the justification of the filamentary current model in application to the substorm dipolarizations). Also, in the current version we avoid interpreting magnetospheric observations made too close (within 1 R_E) to the current filament axis, that is, in the regions of strong B field gradients. Because of that, when solving the inverse problem, we basically rely upon the spacecraft measurements made in the middle of the dipolarized region (where the filamentary model predicts a plateau type B_z profile). In agreement with Figures 3–5, the basic information is taken from g12 and P5 spacecraft for activation #2 and from g13 and g14 spacecraft for activation #3. As concerns the DRP system, which is much less investigated observationally compared to the SCW, we model it by a R2-like filamentary loop with the equatorial current at 13 R_E. Its azimuthal boundaries are derived from the results of midlatitude magnetogram inversion shown in Figure 2. In a similar way, we place a westward current ring at 5 R_E to model the symmetric ring current. The optimal solution (minimization of the RMS deviation) is sought for the fit function including

$$F = K_{\rm st} \sum \left((\mathrm{d}X_o/C_i - \mathrm{d}X_m)^2 + (\mathrm{d}Y_o/C_i - \mathrm{d}Y_m)^2 \right) + K_{\rm sc} \sum \left(\mathrm{d}B_{Zo} - \mathrm{d}B_{Zm} \right)^2$$

where the summation is performed over $N_{\rm st} = 19$ stations and over $N_{\rm sc}$ spacecraft (using those 1 or 2 probes, which appear inside of the dipolarized region), $C_i = 1.5$ is the induction correction factor (see discussion in *Sergeev et al.* [2014] and *Chu et al.* [2014]) and indexes o and m correspond to observed and modeled values. The weights $K_{\rm st}$ and $K_{\rm sc}$ are introduced to make the contribution to the fit function obtained from a few spacecraft comparable to the contribution from many ground stations (here we used $K_{\rm st} N_{\rm st} = K_{\rm sc} N_{\rm sc}$, with $K_{\rm st} + K_{\rm sc} = 1$).

We run the inversion procedure between 0500 and 0600 UT using 0456 UT as a reference level. Usually, we find a distinct global minimum as a result of the merit function minimization. Figure 8 shows a typical comparison of observed and modeled data, which confirms that both the distribution of midlatitude variations (X and Y components) and the dipolarization magnitudes dB_z inside the SCW sector in the magnetosphere are reproduced well by the model. (Similar panels are shown for the entire modeled time period in Animation S2.) Note that in this version of modeling runs we do not include data from spacecraft located outside the SCW, because our ultimate goal is an accurate estimation of the SCW parameters. Although the weights from spacecraft were much higher and the number of spacecraft was changing during subsequent time

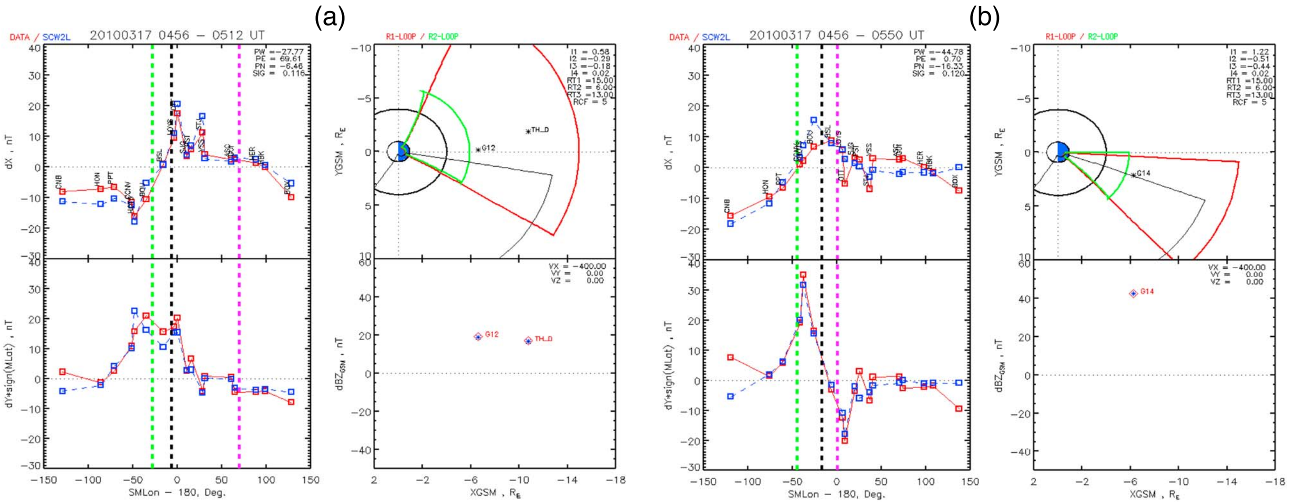

Figure 8. Illustration of inversion results for the epochs at (a) 0512 UT and at (b) 0550 UT near the maxima of dipolarizations #2 and #3. Observed (red) and modeled (blue) values are compared: Figures 8a and 8b (left column) shows X and Y ground perturbations, and the dipolarization at magnetospheric spacecraft is shown on Figures 8a and 8b (bottom right). Figures 8a and 8b (top right) shows equatorial projections of three current loops (red: R1, green: R2, and black: DRP) as well as of magnetospheric spacecraft observing the dipolarization. See the entire simulated time sequence in Animation S2.

steps due to the changing SCW edges location, their effects on the results were minor: comparison of subsequent frames in Animation S2 assures us that agreement between model and observations was good, both at midlatitudes and at the magnetospheric spacecraft and that it did not change considerably across the stepwise N_{sc} changes. The uncertainty in the I2 intensity and I2/I1 ratio, related to the varying RT2 locations, was small (about 10%), reflecting the relatively weak I2 current and stabilizing role of the midlatitude input.

Figure 9 shows the time variation of the SCW2L parameters. Comparison with results from the ground magnetogram inversion shown in Figure 2 confirms that adding the dipolarization amplitude in the magnetosphere to the analyses changes the estimated magnitude of the net SCW current (Figure 9, top): its intensity is now twice as large in activation #3 compared to #2, whereas they had comparable peak values of 0.5–0.6 MA when using only the ground data (shown here by the green curve). During the growth of the SCW current there are some differences between the runs made with different reference times (at 0456, blue curve, or at 0536 UT, black curve), however, the peak values are comparable in both runs, which makes it easier to compare the SCW2L results with AMPERE's results.

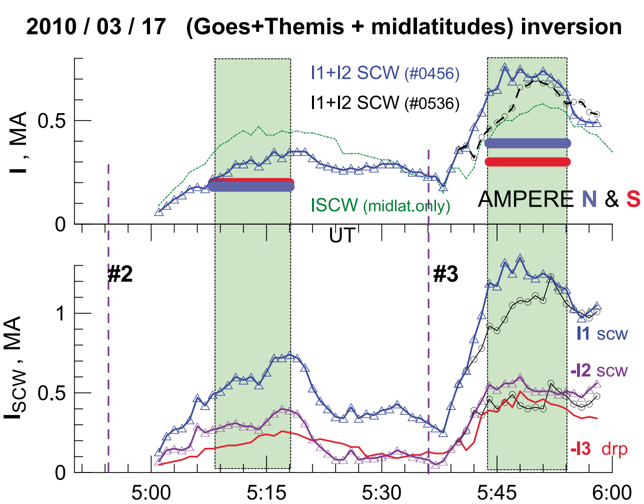

Figure 9. (bottom) Time variations of the SCW2L current components in different runs obtained from magnetogram inversion using the SCW2L model with the additional DRP current loop. (top) Variations of the net current (I1 + I2) are compared to the net SCW currents estimated from AMPERE observations made separately in the two hemispheres. Two runs made with different reference times (at 0456, blue curve, or at 0536 UT, black curve) are shown for comparison.

The most interesting aspect is the comparison of the net SCW currents in Figure 9 (top), which can be more easily separated from other global FAC components found in the ionospheric observations. The representative AMPERE values discussed in section 3 are shown by horizontal colored bars on the plots for 10 min windows close to the maxima of activations #2 and #3. In agreement with our inversion results, they show roughly twofold increase from activation #2 to #3, but the absolute values of the net current inferred from

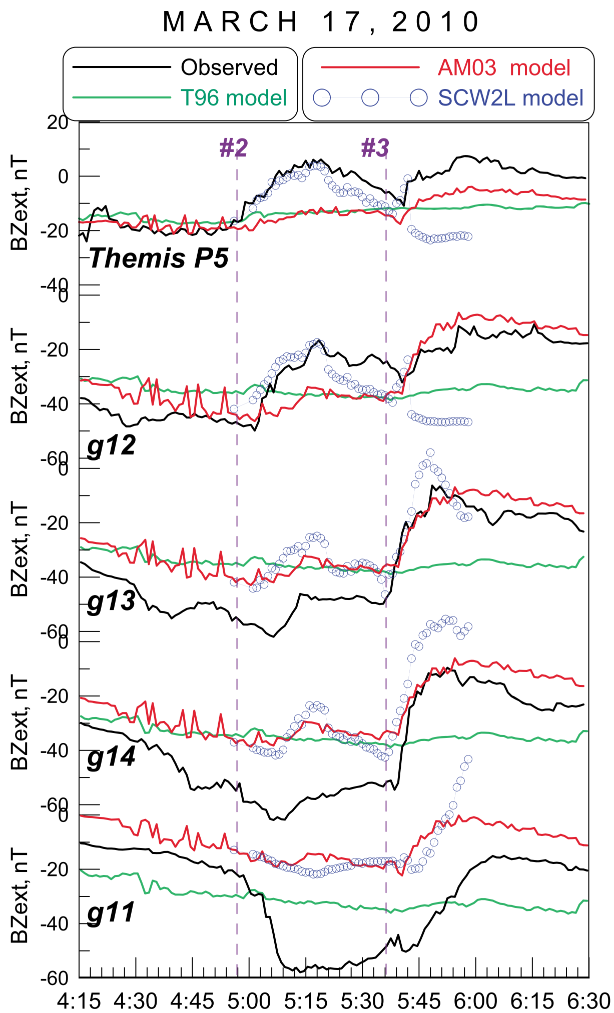

Figure 10. Comparison of B_Z component variations (with International Geomagnetic Reference Field subtracted) observed by five key spacecraft with those modeled using T96, AM03, and the modified SCW2L models.

AMPERE, 0.2 and 0.3–0.4 MA, respectively, are nearly twice smaller than their values derived from magnetospheric and midlatitude observations in this section.

5. SCW Role in Magnetospheric Configuration Changes

To evaluate how well the SCW2L simulates the magnetic field changes in the nightside inner magnetosphere, we test it against two other (Tsyganenko-96, T96, and Adaptive Model-03, AM03) models. The AM03 is the most advanced version of adaptive model among those described in *Kubyshkina et al.* [2011]. The adaptive modeling is a method of fitting models to spacecraft observations in specific events. It utilizes the same smooth functions as the T96 model to describe contributions to the observed field from principal sources but finds free input parameters by minimizing the RMS deviation of the model output from the field observed at each time during that specific event. In addition, the AM03 model allows one to vary the neutral sheet tilt and include thin current sheets, as described in *Kubyshkina et al.* [2011].

We run AM03 for the time interval 0400–0630 UT by using solar wind OMNI data and magnetic data from eight spacecraft (four GOES spacecraft, THEMIS P3, P4, and P5 probes, and Artemis AP2). Results for the B_z component (representing dipolarization) are shown in Figure 10, whereas all field components at all spacecraft are illustrated in the Figure S3. Compared to predictions of the standard T96 model, which responds to solar wind variations but shows no internal substorm-related variations (green curves), the AM03 model (red curves) reproduces dipolarizations #2 and #3. However, using large-scale smooth functions to model the currents, the AM03 fits equally observations made both inside and outside the dipolarized region. As a result of this tradeoff, the dipolarization amplitude in the AM03 (red curve) is smaller than that observed by the spacecraft (black curve) inside the dipolarization (e.g., g12 and P5 during #2, and g13, g14, g11 at #3). At the same time, AM03 also shows a similar dipolarization at the spacecraft that stays outside the dipolarized region and does not observe any dipolarization or even detects an opposite effect (like g11 during the activation #2). The nice reproduction of two dipolarizations in this event is merely due to the fact that more spacecraft happen to be located inside the dipolarization region than outside.

Regarding the SCW2L model, it presents the perturbations from the reference level at 0456 UT rather than the total field. Being interested in the comparison of the dipolarization amplitudes in the inner magnetosphere, in Figure 10 we arbitrarily chose to draw the SCW2L perturbations starting from the B_Z component level of the AM03 model taken at 0456 UT. As seen from this plot, the SCW2L-modeled variations nicely reproduce the dipolarization amplitude at those spacecraft which stay inside the dipolarization region. One exception is a sharp B_z drop at P5 and g12 at 0543 UT, which is caused by a sudden large westward shift of SCW eastward edge (Pe) in the ground inversion results (Figure 2) used in our simulation. As discussed in section 2.1 this artificial feature appears due to the coexistence of the preexisting (postmidnight) wedge with the quickly growing new (premidnight) wedge, which we attempted to interpret by the model consisting of only one current wedge. This certainly can be improved by adding the second wedge (which is beyond the scope of this work).

We also note poor agreement before 0545 UT at the g11 spacecraft that stays in the premidnight sector occupied by the DRP system: the modeled amplitude of B_z depression is much smaller than the observed $\sim$ 20 nT depression. Note that the observed B_z variation at g11 was not used as input in our modeling, so the DRP current amplitude was determined entirely by ground perturbations. This discrepancy clearly shows a need to modify the DRP model, which can be a subject for future study.

6. Discussion

Due to extraordinary spacecraft coverage in a wide region of the magnetotail, conjugate to a dense network of ground-based magnetometers, and as a result of the distinct step-like nature of the 17 March 2010 substorm, we were able to combine these different data sets and present a synthesis of the azimuthal spatial dynamics of magnetospheric activity. We were also able to test and compare different ways to represent, monitor, and model the substorm current system.

The step-like development of substorms, known under the names of "multiple substorm onsets," "multiple substorm activations," or "microsubstorms," was a subject of intense studies in 1970s (see, e.g., [*Pytte et al.*, 1976], and a review in [*Sergeev et al.*, 1996b]), and this topic continues to attract attention [*Kadokura et al.*, 2002; *Lyons et al.*, 2012]. In section 2 we demonstrated that the SCW prediction based on midlatitude magnetogram inversion makes it possible to organize various substorm signatures in the midtail and near tail, indicating that the activity has an azimuthal structure, with different sectors activated at different times in the course of a substorm. Although these connections have been known from previous studies which focused on isolated aspects of the whole picture, we were able for the first time to synthesize them into a general picture in one substorm case study. This event nicely confirms how many different phenomena, such as the dipolarizations, fast flows, plasma sheet thinning/expansion, depleted plasma tubes, and injections, are mutually related and coherently organized in space. Current understanding relates these features to a stepwise localized event of magnetotail magnetic field reconnection, which extracts the magnetic energy stored in the midtail and converts it to the energy in flow bursts, which subsequently feeds the substorm dipolarization and plasma injections [*Birn and Hesse*, 2014; *Angelopoulos et al.*, 2013; L. Kepko et al., submitted manuscript, 2014].

Our study illustrates once again that the magnetogram inversion technique [*Sergeev et al.*, 1996a; *Chu et al.*, 2014] provides a useful tool to quantitatively monitor the spatial dynamics and intensity of substorm currents in the near tail, in a way that is better than other methods, from our perspective. Based on the comparison between the inferred SCW dynamics and injection/dipolarization onsets observed at magnetospheric spacecraft (section 2 and Figure 4), the accuracy of predicting the azimuthal boundaries (from association between the midlatitude SCW edge location and spacecraft location at the dipolarization onset for delayed dipolarizations in Figure 4) is roughly 1 h MLT, in our case.

To follow the substorm development, in this paper we use for the first time the SCW2L model, complemented by a simple DRP model, and use both magnetospheric and ground midlatitude magnetic variations as the input to the inversion algorithm. Compared to the traditional inversion, it allows us to infer both R1 and R2 components of the current system, consistent with dipolarization amplitudes observed in the near tail [*Sergeev et al.*, 2014]. Agreement between the modeled and observed B_z variations is generally good (Figure 9), except for two features. As briefly discussed in section 5, the disagreement between observed and predicted B_z variations at g12 and P5 after 0545 UT is not surprising. In this situation, we used a model with one wedge, when there was an obvious coexistence of a new premidnight wedge, quickly growing on top of the slowly decaying postmidnight wedge. This is not a principal deficiency, as adding a second wedge to the model can amend it. In this work it was not pursued because such detail is beyond our current goals and because it could not be fully automated. Another disagreement between model and observation concerns the inability of the simple (one R2 sense loop) DRP model to reproduce the deep ($\sim$ -20 nT) B_z component depression observed at g11 between 0500 and 0530 UT (Figure 9). We recall that g11 data were not used as input in finding the DRP total current, whose intensity was defined primarily from the ground midlatitude perturbations. Experiments that add g11 data as input, showed that such a simple one-loop system is unable to reproduce simultaneously both spacecraft and ground perturbation amplitudes. Like in the case of using a single-loop model for the SCW [*Sergeev et al.*, 2011], we conclude that the DRP current system model needs to be significantly improved. However, the spacecraft coverage of the DRP system is not sufficient for that goal, so it is relegated as a task for future studies.

In our study we used two different data-fitted models, SCW2L and AM03, to model the magnetic variations in the magnetosphere during substorm development. The SCW2L model clearly outperforms the adaptive model in reproducing the large dipolarization-related variations of B_z component characterizing the field dipolarization and stretching during substorms. This is not surprising, taking into account that the SCW2L was specially designed for that goal. A good quantitative reconstruction of large-scale reconfigurations during dipolarizations make the SCW2L a useful tool for the substorm-related field mapping and related issues. The advantage of the AM03 is that it does not require a reference level and provides a continuous data-based representation of the total field for both substorm and nonsubstorm periods.

Also, we compared for the first time the magnetospheric view of the substorm current wedge (based on the SCW2L model) with variations of the large-scale field-aligned currents, independently provided by the AMPERE project. Both methods have caveats and difficulties, and their comparison is not a trivial task. In the case of AMPERE, the limited spatial (2 h MLT) and temporal resolution (∼ 10 min) clearly limit the studies of time-varying mesoscale (SCW-like) systems, and the uneven coverage is also an issue. However, our major and principal problem is how to distinguish and separate the part of the currents related to the mesoscale SCW current system from the large-scale FAC system related to magnetospheric convection (regions 1 and 2 Iijima-Potemra system) and other mesoscale components. One way is to analyze the FAC pattern change after the onset of strong activations. The total FAC pattern observed at 0508UT in Figure 6c gives a qualitative view of such changes (recall that in dark northern auroral zone there were very weak FACs prior to the onset of activation #2). On the nightside we clearly see the quadrupolar current system consisting of poleward R1-like FACs combined with (slightly less intense and more equatorward) R2-like FACs in the same sector. This is consistent with results by *Clausen et al.* [2013] and *Anderson et al.* [2014] who showed that the nightside FACs dominate during the substorm expansion phase, that here the R1- and R2-current systems grow in concert with each other, and that such behavior is at least not uncommon. In contrast to these studies, recently *Connors et al.* [2014] demonstrated a single (R1) loop SCW in a case study using AMPERE and ground-based data, and *Gjerloev and Hoffman* [2014] discussed a possibility of two azimuthally separated wedge current systems to interpret the auroral zone currents near the time of substorm peak. Therefore, whereas the AMPERE results generally support a quadrupolar FAC system, with the R1 system dominating over the R2-like system and providing the net R1-type SCW-like current, extensive documentation of the current system's development is clearly warranted.

Identification of a spatial domain occupied by the SCW system is a next problem. *Murphy et al.* [2013] found that the major increases of westward electrojet in the auroral zone are observed at stations located in a longitude sector between the peaks of upward and downward currents, which fits the expectation from SCW-type current system. Following their finding, we attempt to identify the SCW-related part based on the signatures of the net (meridionally averaged) FACs. Similarly to Murphy et al., in two activations occupying different MLT sectors we found that the peaks of those net FACs nearly correspond (within 1 h MLT) to the SCW edge locations, computed from the midlatitude magnetogram inversion, and that these net currents have the R1-like polarity (Figure 7b). Besides that, the total upward and downward currents appear to have comparable values in two hemispheres. These facts motivated us to choose the total net FAC values as the most reliable SCW characteristics to be used in quantitative comparisons.

According to ionospheric estimates, the net SCW-related FAC appears to be smaller (about one half) of the SCW2L net current. A number of factors exist that can diminish the difference. Particularly, the low spatial resolution inherent to the AMPERE method, most likely, results in currents smaller than in reality, as recently discussed by *Korth et al.* [2004] and *Merkin et al.* [2013]. In the magnetogram inversion method, some ambiguity exists with regard to estimating the contribution of the induction currents. In our method we applied the correction coefficient $C_i = 1.5$. *Chu et al.* [2014] recently discussed this and noticed that at individual stations such factors can be somewhat larger (1.6 to 2), which would result in smaller values of the net SCW2L current. In view of all these uncertainties, the agreement within a factor 2 between two independent estimates can be considered quite encouraging and may stimulate further work in this direction.

7. Conclusions

The updated SCW model extends previous work on such models and provides a new understanding of substorm and magnetotail dynamics and the coupling between the ionosphere and magnetosphere. At the same time, it provides an attractive avenue for further research and for use as a diagnostic tool. In this paper we benefited from unprecedented spacecraft and instrumental coverage and the isolated nature and distinct stepwise development of the isolated 17 March 2010, substorm. This allowed us to investigate the SCW development and validate the new SCW2L model (with the quadrupolar field-aligned currents) with spacecraft observations in the magnetosphere, with AMPERE observations of global FACs, and by comparing its performance to another data-based magnetospheric model.

The unprecedented data coverage also allowed us to demonstrate the close spatiotemporal relationship of the SCW with many other essential signatures of substorm activity in the magnetotail, including tailward flux transport in the more distant tail, flow bursts, and disruptions of the thin current sheet in the near tail, and especially the dipolarizations and particle injections at geosynchronous orbit. This case study nicely illustrates the sectorial organization of activity in the magnetotail, which is confined to azimuthally localized sectors and expands in stepwise way to new sectors, presumably reflecting the stepwise cross-tail evolution of the localized reconnection process. We confirm that the ground-based SCW diagnostics makes it possible to reconstruct and organize the azimuthal spatiotemporal substorm development pattern with an accuracy better than 1 h MLT in case of medium substorms.

The AMPERE-based study of the global field-aligned current distribution supports the SCW2L model and shows in our case that (a) the SCW-related FAC system consists of simultaneously activated R1- and R2-type currents with similar intensities in both hemispheres, (b) their net currents have the R1-sense polarity, and (c) locations of the net current peaks are consistent with those inferred from midlatitude magnetic variations. Moreover, by combining the magnetospheric and ground midlatitude magnetic variations as input to the SCW2L model, we evaluated the intensities of total SCW R1- and R2-like current loop and found that its net current agrees within a factor 2 with AMPERE's results. Finally, we ran the adapted magnetospheric model and showed that the SCW2L model outperforms it in predicting the magnetic configuration changes during substorms. These results confirm a good potential for applications and a need to further develop the SCW2L model.

Acknowledgments

This event was first selected for a detailed study at the meeting of the International Space Science Institute team "The substorm current wedge," we thank the team members for stimulating discussions. Initial analyses has also been a part of the EU FP7 ECLAT project. The work of SPbU group on the SCW2L validation has been supported by the Russian Science Foundation grant 14-17-00072. We thank C.W. Carlson and J.P. McFadden for use of ESA data; K.H. Glassmeier, U. Auster, and W. Baumjohann for the use of FGM data provided under the lead of the Technical University of Braunschweig and with financial support through the German Ministry for Economy and Technology and the German Center for Aviation and Space (DLR) under contract 50 OC 0302; the work by V.A. was partly supported by THEMIS contract NAS5-02099. J.V.R. was supported by the GOES-R Risk Reduction Program. S.E.M. was supported on Science and Technology Funding Council (STFC, UK) grant ST/K001000/1. J.C.C. was supported by an STFC studentship. We thank H. Bysal of NOAA NSOF for providing the raw GOES-13 data for this study. The GOES data used in this study are available upon request.

Larry Kepko thanks two anonymous reviewers for their assistance in evaluating this paper.

References

Anderson, B. J., H. Korth, C. L. Waters, D. L. Green, V. G. Merkin, R. J. Barnes, and L. P. Dyrud (2014), Development of large-scale Birkeland currents determined from the Active Magnetosphere and Planetary Electrodynamics Response Experiment, *Geophys. Res. Lett.*, *41*, 3017–3025, doi:10.1002/2014GL059941.

Angelopoulos, V., et al. (2013), Electromagnetic energy conversion at reconnection fronts, *Science*, *341*(6153), 1478–1482, doi:10.1126/science.1236992.

Birn, J., and M. Hesse (2014), The substorm current wedge: Further insights from MHD simulations, *J. Geophys. Res. Space Physics*, *119*, 3503–3513, doi:10.1002/2014JA019863.

Birn, J., M. F. Thomsen, J. E. Borovsky, G. D. Reeves, D. J. McComas, and R. D. Belian (1997), Characteristic plasma properties during dispersionless substorm injections at geosynchronous orbit, *J. Geophys. Res.*, *102*, 2309–2324, doi:10.1029/96JA02870.

Chu, X., et al. (2014), Development and validation of inversion technique for substorm current wedge using ground magnetic field data, *J. Geophys. Res. Space Physics*, *119*, 1909–1924, doi:10.1002/2013JA019185.

Clausen, L. B. N., S. E. Milan, J. B. H. Baker, J. M. Ruohoniemi, K.-H. Glassmeier, J. C. Coxon, and B. J. Anderson (2013), On the influence of open magnetic flux on substorm intensity: Ground- and space-based observations, *J. Geophys. Res. Space Physics*, *118*, 2958–2969, doi:10.1002/jgra.50308.

Connors, M., R. L. McPherron, B. J. Anderson, H. Korth, C. T. Russell, and X. Chu (2014), Electric currents of a substorm current wedge on 24 February 2010, *Geophys. Res. Lett.*, *41*, 4449–4455, doi:10.1002/2014GL060604.

Gjerloev, J. W., and R. A. Hoffman (2014), The large-scale current system during auroral substorms, *J. Geophys. Res. Space Physics*, *119*, 4591–4606, doi:10.1002/2013JA019176.

Hanser, F. A. (2011), *EPS/HEPAD calibration and data handbook*, *Tech. Rep. GOESN-ENG-048D*, Assurance Technology Corporation, Carlisle, Mass. [Available at http://www.ngdc.noaa.gov/stp/satellite/goes/documentation.html.]

Horning, B., R. McPherron, and D. Jackson (1974), Application of linear inverse theory to a line current model of substorm current systems, *J. Geophys. Res.*, *79*(34), 5202–5210.

Ieda, A., et al. (2008), Longitudinal association between magnetotail reconnection and auroral breakup based on Geotail and Polar observations, *J. Geophys. Res.*, *113*, A08207, doi:10.1029/2008JA013127.

Kadokura, A., A.-S. Yukimatu, M. Ejiri, T. Oguti, M. Pinnock, and P. R. Sutcliffe (2002), Detailed analysis of a substorm event on 6 and 7 June 1989: 2. Stepwise auroral bulge evolution during expansion phase, *J. Geophys. Res.*, *107*(A12), 1480, doi:10.1029/2001JA009129.

Korth, H., B. J. Anderson, M. J. Wiltberger, J. G. Lyon, and P. C. Anderson (2004), Intercomparison of ionospheric electrodynamics from the Iridium constellation with global MHD simulations, *J. Geophys. Res.*, *109*, A07307, doi:10.1029/2004JA010428.

Kubyshkina, M., V. Sergeev, N. Tsyganenko, V. Angelopoulos, A. Runov, E. Donovan, H. Singer, U. Auster, and W. Baumjohann (2011), Time-dependent magnetospheric configuration and breakup mapping during a substorm, *J. Geophys. Res.*, *116*, A00I27, doi:10.1029/2010JA015882.

Lyons, L. R., Y. Nishimura, X. Xing, A. Runov, V. Angelopoulos, E. Donovan, and T. Kikuchi (2012), Coupling of dipolarization front flow bursts to substorm expansion phase phenomena within the magnetosphere and ionosphere, *J. Geophys. Res.*, *117*, A02212, doi:10.1029/2011JA017265.

McPherron, R., C. Russell, M. Kivelson, and P. Coleman Jr. (1973), Substorms in space: The correlation between ground and satellite observations of the magnetic field, *Radio Sci.*, *8*(11), 1059–1076, doi:10.1029/RS008i011p01059.

McPherron, R. L., T.-S. Hsu, J. Kissinger, X. Chu, and V. Angelopoulos (2011), Characteristics of plasma flows at the inner edge of the plasma sheet, *J. Geophys. Res.*, *116*, A00I33, doi:10.1029/2010JA015923.

Merkin, V. G., B. J. Anderson, J. G. Lyon, H. Korth, M. Wiltberger, and T. Motoba (2013), Global evolution of Birkeland currents on 10 min timescales: MHD simulations and observations, *J. Geophys. Res. Space Physics*, *118*, 4977–4997, doi:10.1002/jgra.50466.

Murphy, K. R., I. R. Mann, I. J. Rae, C. L. Waters, H. U. Frey, A. Kale, H. J. Singer, B. J. Anderson, and H. Korth (2013), The detailed spatial structure of field-aligned currents comprising the substorm current wedge, *J. Geophys. Res. Space Physics*, *118*, 7714–7727, doi:10.1002/2013JA018979.

Nagai, T. (1982), Observed magnetic substorm signatures at synchronous altitude, *J. Geophys. Res.*, *87*, 4405–4417.

Pytte, T., R. L. McPherron, M. G. Kivelson, H. I. West Jr., and E. W. Hones Jr. (1976), Multiple-satellite studies of magnetospheric substorms: Radial dynamics of the plasma sheet, *J. Geophys. Res.*, *81*(34), 5921–5933, doi:10.1029/JA081i034p05921.

Sergeev, V. A., T. Bosinger, R. D. Belian, G. D. Reeves, and T. E. Cayton (1992), Drifting holes in the energetic electron flux at geosynchronous orbit following substorm onset, *J. Geophys. Res.*, *97*, 6541–6552.

Sergeev, V. A., L. I. Vagina, R. D. Elphinstone, J. S. Murphree, D. J. Hearn, L. L. Cogger, and M. L. Johnson (1996a), Comparison of UV optical signatures with the substorm current wedge predicted by an inversion algorithm, *J. Geophys. Res.*, *101*(A2), 2615–2627.

Sergeev, V. A., T. I. Pulkkinen, and R. J. Pellinen (1996b), Coupled-mode scenario for the magnetospheric dynamics, *J.Geophys.Res.*, *101*, 13,047–13,065.

Sergeev, V. A., N. A. Tsyganenko, M. V. Smirnov, A. V. Nikolaev, H. J. Singer, and W. Baumjohann (2011), Magnetic effects of the substorm current wedge in a “spread-out wire” model and their comparison with ground, geosynchronous, and tail lobe data, *J. Geophys. Res.*, *116*, A07218, doi:10.1029/2011JA016471.

Sergeev, V. A., A. V. Nikolaev, N. A. Tsyganenko, V. Angelopoulos, A. V. Runov, H. J. Singer, and J. Yang (2014), Testing a two-loop pattern of the substorm current wedge (SCW2L), *J. Geophys. Res. Space Physics*, *119*, 947–963, doi:10.1002/2013JA019629.

Singer, H. J., W. J. Hughes, C. Gelpi, and B. G. Ledley (1985), Magnetic disturbances in the vicinity of synchronous orbit and the substorm current wedge: A case study, *J. Geophys. Res.*, *90*, 9583–9589.

Yang, J., F. R. Toffoletto, R. A. Wolf, S. Sazykin, P. A. Ontiveros, and J. M. Weygand (2012), Large-scale current systems and ground magnetic disturbance during deep substorm injections, *J. Geophys. Res.*, *117*, A04223, doi:10.1029/2011JA017415.

